Journal of Materials Science: Materials in Engineering

ORIGINAL PAPER Open Access

Enhanced photo-induced optical activity of crisscrossed self-organized gratings in photosensitive nanolayers by introducing bi-periodicity

Arashmid Nahal[1,2*] and Ozra Kiasatfar[1]

Abstract

In the present work, the enhancement of photoinduced optical activity in a photosensitive nanolayer of AgCl doped by Ag nanoparticles, using bi-periodic crisscrossed self-organized periodic nanostructures (C-SPNs) is achieved. We found that the formation of two non-identical SPNs (i.e., with different periods), which crisscrossed each other, enhances the rotation of the polarization plane of the linear polarized probe beam, compared to the case when the two nanostructures are identical (i.e., having the same period). The difference in periods of the two C-SPNs increases the anisotropy of the medium, which in turn boosts the optical chirality produced by the formation of complex crisscrossed gratings made of Ag nanoparticles. The angle between the two gratings can be a control parameter for the amount and sign of rotation of the polarization plane of the probe beam. The enhanced optical activity of the bi-periodic C-SPNs, compared to the identical C-SPNs, can be attributed to the formation of more intricate chiral building blocks at the intersections of the two gratings.

Keywords Bi-periodicity, Self-organized nanostructures, Optical chirality, Light-sensitive thin films, Silver nanoparticles, Optical rotation dispersion

Introduction

Induced optical activity in plasmonic photonic materials has garnered significant attention from research groups in recent years (Kuwata-Gonokami et al. 2005; Jefimovs et al. 2005; Valev et al. 2013; Kildishev et al. 2013; Kalachyova et al. 2015). This interest stems from its potential applications in optoelectronics and integrated optics, where it serves as a photonic element for controlling light beam polarization, modulation, or switching (Barron 2004; Schaferling 2017). The optical active medium rotates the plane of polarization of a passing-through probe beam due to two structural and geometrical properties: (i) anisotropy of the photonic material and (ii) optical chirality of elements formed within the medium. Increasing the anisotropy of the medium enhances optical chirality (Murai et al. 2011; Nahal and Talebi 2014; Nahal and Kashani 2017).

A pioneering study (Nahal et al. 1998) demonstrated that irradiating photosensitive slab waveguide thin films like AgCl (doped with silver nanoparticles, Ag-NPs) using circularly polarized laser beams induces optical activity. The excitation of TE_n-modes in the AgCl waveguide layer occurs due to the scattering of incident light by Ag-NPs coated on the surface. The excited running modes interfere with the incident polarized beam (Fig. 1a), leading to the migration of metallic Ag-NPs into the minima of

*Correspondence:
Arashmid Nahal
nahal@ut.ac.ir
[1] Photonic Materials Research Laboratory, Department of Physics, College of Science, University of Tehran, Tehran 14399-55961, Iran
[2] Optical Metrology Research Laboratory, Department of Physics, College of Science, University of Tehran, Tehran 14399-55961, Iran

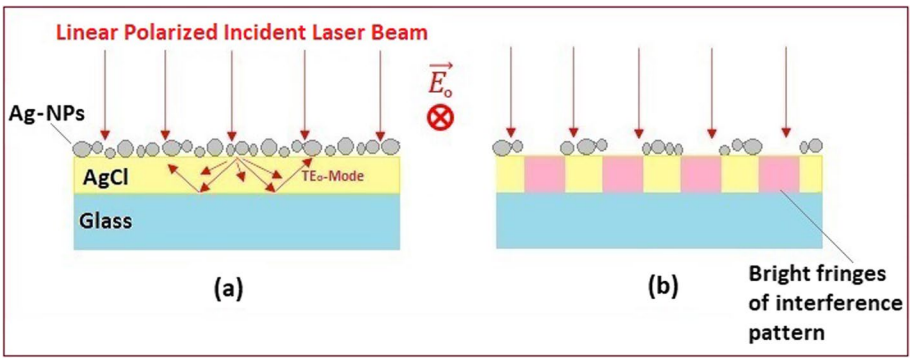

Fig. 1 A scheme demonstrating the interaction of a linear polarized incident laser beam with AgCl thin film on a glass substrate (**a**) covered by an island-like layer of silver nanoparticles (Ag-NPs). Some part of the incident light scatters into the AgCl layer and propagates as a TE_n-mode of the slab waveguide; **b** migration of Ag-NPs to the minima of the interference pattern formed by interference between incident light and propagating TE_n-modes. $\vec{E}_o$ is the polarization vector of the incident laser beam

the interference pattern, forming self-organized periodic nanostructures (SPNs) according to the interference field (Fig. 1b) (Nahal and Talebi 2014; Ashkin 1970; Ageev and Miloslavsky 1995; Ageev et al. 1997; Nahal et al. 2006; Kashani and Nahal 2017). The generated SPN acts as an entrance gate for modes into the AgCl slab waveguide. An increase in the intensity of the modes enhances the interference pattern contrast (Kashani and Nahal 2017) leading to the acceleration of migration of Ag-NPs into the minima of the interference pattern. The better the SPN, the more intense the TE_n-modes, resulting in an iterative process. This positive feedback mechanism (PFB) leads to the self-improvement of the generated SPNs. For this reason, sometimes they are called "self-organized" nanostructures.

Under linearly polarized incident light, the SPNs form grating-like assemblies of Ag-NPs with a domain structure (Fig. 2). Small-angle scattering (SAS) patterns have been extensively used to study this domain structure (Ageev et al. 1997; Miloslavsky et al. 1998; Miloslavsky

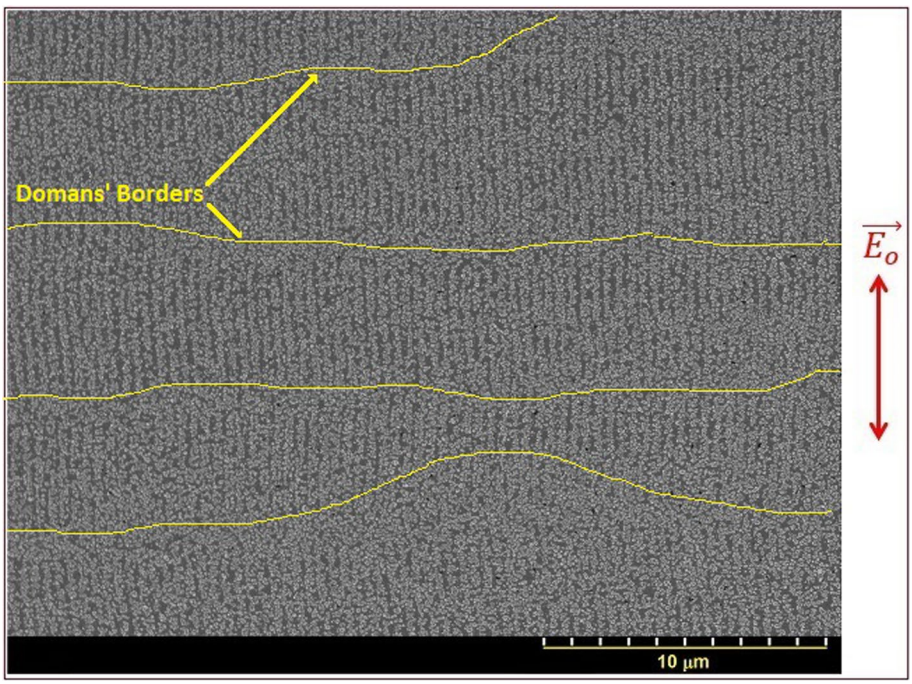

Fig. 2 SEM image of a self-organized periodic nanostructure (SPN) formed by a linearly polarized He-Ne laser beam with a power of 5 mW. The vector $\vec{E}_o$ is the polarization vector of the incident laser beam. Borders of some domains are highlighted by yellow lines and indicated by arrows on the image

et al. 1999). Direct double autocorrelation of an AFM image of an SPN formed by linear polarization (Fig. 3a) reveals that each domain is slightly tilted relative to the main SPN direction (Fig. 3b). Scattering of running modes within these domains results in the observed SAS pattern. Similar self-organized periodic nanostructures are observed in different photonic materials under ultrafast laser beam irradiation (Zhang et al. 2019; Zhang et al. 2019; Zhang et al. 2023). But they mostly function in the near-IR region of the spectrum.

These linear SPNs, also known as spontaneous gratings, originate from the scattering of incident light by Ag-NPs and the excitation of TE_n-modes within the AgCl layer. Further investigations have shown that elliptical (Miloslavsky et al. 1998) and circular (Miloslavsky et al. 1999; Ageev et al. 2000) polarized incident laser beams (typically a He-Ne laser beam, $\lambda_R = 632.8$ nm, power = 5 mW) lead to the formation of complex structures and chiral silver nanoparticles, inducing enhanced optical activity in the irradiated *Ag/AgCl/Glass* photosensitive system (Nahal et al. 1998).

In all the cases mentioned earlier, the information related to the sign and polarization state of the incident light is recorded by the formed SPN (Nahal and Talebi 2014; Nahal and Kashani 2017; Nahal et al. 1998). Specifically:

- An SPN formed by left-handed circular (or elliptical) polarized incident light can rotate linearly polarized probe light to the left.
- An SPN formed by right-handed circular (or elliptical) polarized incident light can rotate linearly polarized probe light to the right.
- In the case of elliptically polarized incident light, the degree of ellipticity of the polarization serves as a control parameter for the amount of rotation (Nahal and Talebi 2014).

Additional effective methods for inducing optical activity in photosensitive thin films include the following:

- Off-normal incidence of the laser beam (Hirbodvash et al. 2015).
- Formation of two identical crisscrossed linear SPNs (referred to as mono-periodic SPNs) with different angles between them (angle α) (Nahal and Kashani 2017).
- Simultaneous excitation of TE_0 and TE_1 modes in thick photosensitive *Ag/AgCl/Glass* systems (Nahal et al. 2019).

Our studies (Nahal and Kashani 2017) show that the crisscrossed mono-periodic SPNs exhibit the highest optical activity compared to other mentioned methods. The common factor between the last two methods (cases (ii) and (iii)) is the *bi-periodicity* of the produced SPNs. *Bi-periodicity* refers to the co-existence of two generated SPNs with two distinct periods within the *Ag/AgCl/glass* system. As previously mentioned, *mono-periodic* SPNs are those formed successively with the same periods.

Based on our results, we conclude that combining *bi-periodicity* and *the crisscrossing* of two SPNs—forming bi-periodic C-SPNs instead of mono-periodic ones—can achieve greater enhancement of induced optical activity. Our present work focuses on the results of this study, and we observed that the optical rotation of bi-periodic C-SPNs is generally 30% higher than that of mono-periodic C-SPNs.

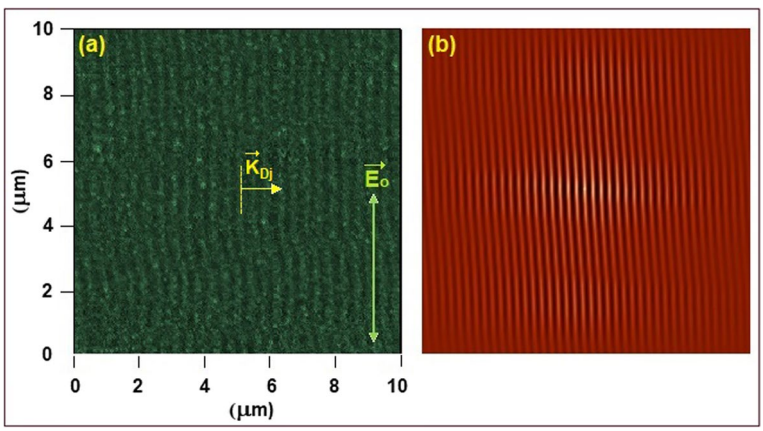

Fig. 3 **a** AFM image of an SPN formed by a linear polarized He-Ne laser beam. $\vec{K}_{Dj}$ is the vector of the *J*th domain. $\vec{E}_o$ is the polarization vector of the incident laser beam; **b** direct double autocorrelation of Fig. 3a for highlighting the domain structure of SPN

Experiments and results

Sample preparation and the experimental setup

Precisely cleaned glass plates (microscope slides with the refractive index of $n_s = 1.52$ and size $25 \times 75 \times 0.8$ mm) were used as substrates. A thin film of AgCl ($n_f = 2.06$) with a thickness of $h_{AgCl} = 50$ nm was coated on the surface of the substrate using the physical vacuum deposition method (PVD) (at pressure: $p = 4 \times 10^{-5}$ torr). Then, a very thin film of silver ($h_{Ag} = 15$ nm) was coated on the AgCl layer using the same PVD method. The AgCl layer thickness was selected near the TE_0-mode cut-off thickness for an asymmetric slab waveguide, based on the dispersion equation governing such waveguides (Tamir 1979). A thicker slab waveguide allows the excitation of higher orders of TE_n-modes, which leads to the formation of more complicated SPNs, which is not easy to deal with (Nahal et al. 2019). Metallic thin films with a thickness of less than 20 nm have an island-like structure made of granular metallic nanoparticles (Fig. 4a, b) and (Kriebig and Vollmer 1995). A granular layer can cause some of the incident light to scatter into the AgCl layer, which can act as a slab waveguide (Fig. 1a).

In our experiments, Ag-NPs coated on the AgCl layer had an average size of approximately $d \approx 21$ nm (inset Table of Fig. 4). For comparison, a thin film of Ag (<20 nm thickness) was also coated on a glass substrate. AFM studies revealed that on the glass substrate, smaller Ag-NPs formed, resulting in a smoother Ag island-like layer (Fig. 4b and inset Table of Fig. 4). This should be related to the difference between the roughness of the substrates and their chemical surface adsorption (Abdi et al. 2010). Chemical adsorption occurs when the adsorbate nanoparticles or molecules are attracted to the surface of the adsorbent by chemical bonds. The most common type of chemical adsorption is called *covalent bonding*. In covalent bonding, the adsorbate nanoparticles share electrons in such a way that they form a chemical bond with the adsorbent, which is the substrate surface in our case.

The *Ag/AgCl/glass* system functions as a photosensitive thin film. The smaller the size of Ag-NPs, the greater the photosensitivity of the system. That is, even with shorter exposure time or lower incident light intensity, one could easily produce an SPN. The migration of metallic Ag-NPs to the minima of the interference pattern occurs due to

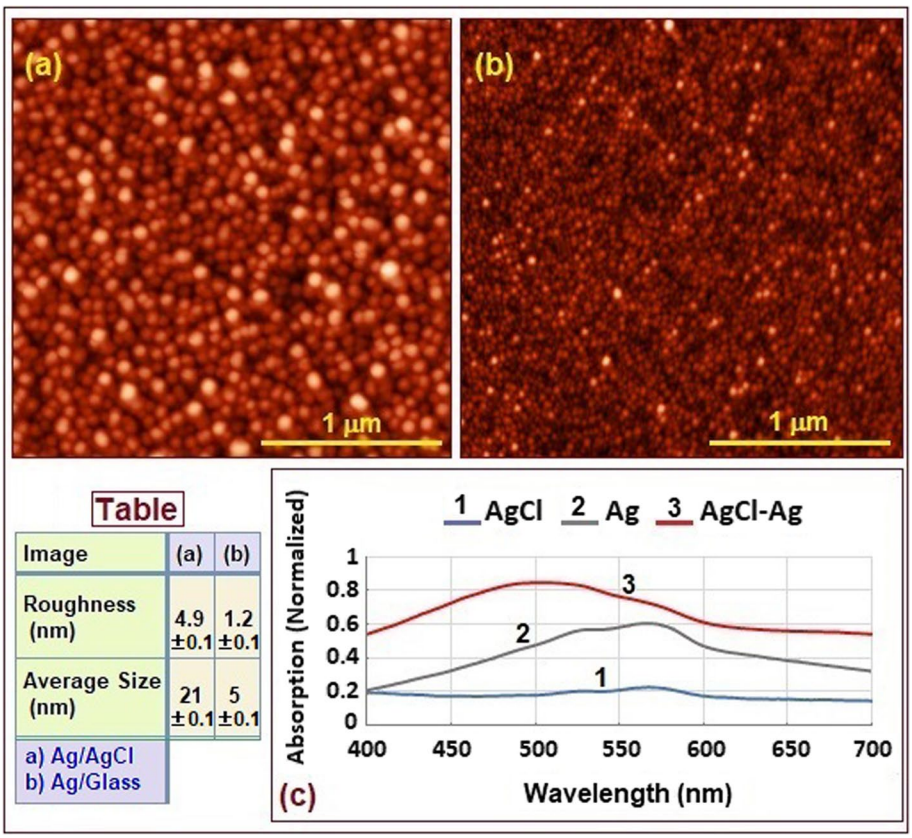

Fig. 4 **a** Silver nanoparticles (Ag-NPs) coated on an AgCl thin film with glass substrate; **b** Ag-NPs coated on a bare glass substrate; **c** absorption spectra of (1) AgCl layer, (2) Ag layer, and (3) AgCl-Ag layer, all on a glass substrate. The inset table contains information about the roughness and average size of Ag-NPs for cases **a** and **b**

the intensity gradient between the minima and maxima of the interference pattern (Fig. 1b). This process minimizes Ag-NPs' total energy, resulting in their stability. Consequently, a periodic structure made of Ag-NPs is generated according to the interference pattern. Since the shape of an interference pattern depends on the wavelength and polarization states of the interfering lights, the formed SPNs inherently encode this information (Nahal and Talebi 2014; Nahal and Kashani 2017; Kashani and Nahal 2017; Nahal et al. 2019; Talebi et al. 2014). Without the AgCl layer, the TE_n-mode cannot be excited, resulting in no interference and no formation of spontaneous periodic nanostructures. A study on Ag, AgCl, and AgCl-Ag thin films for their absorption spectra shows that when the substrate of an Ag island-like layer is AgCl, the surface plasmon resonance absorption peak has a blue shift compared to the case when the substrate is glass (curves 2 and 3 in Fig. 4c). This result indicates that the position of the surface plasmon resonance (SPR) peak in the absorption spectra is influenced not only by the size of the Ag-NPs but also by their interaction with the substrate. The influence of the surrounding medium on the position of the SPR peak in absorption spectra is explained in detail in (Kriebig and Vollmer 1995; Jensen et al. 1999).

To generate an SPN, one should arrange the setup shown in Fig. 5. A screen with a hole in the middle (for passing through the incident laser beam) should be placed in front of the sample to observe the small-angle scattering pattern (SAS). The appearance of the SAS pattern implies the formation of the SPN. The form of the SAS pattern includes information about the polarization state of the incident beam and also about the nanostructure that is forming as a result of the interaction between the laser beam and the photosensitive system [13, 14, 17, and 21].

For producing the first SPN (SPN1) we used a He-Ne laser (P_{RL} = 5 mW, λ_{RL} = 632.8 nm), and for the second

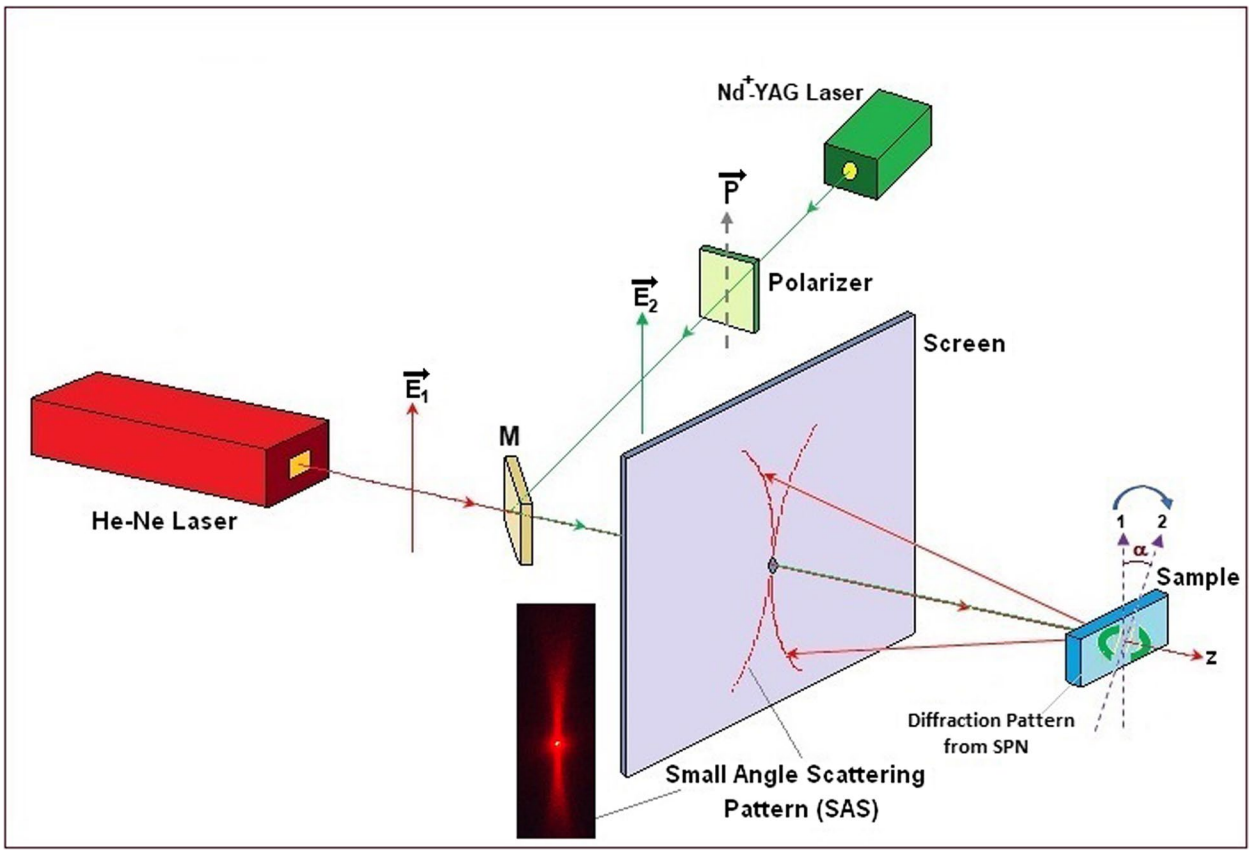

Fig. 5 Experimental setup for producing SPNs with different polarization orientations and wavelengths. $\vec{E}_1$ is the polarization vector of the He-Ne laser beam (P_{RL} = 5 mW, λ_{RL} = 632.8 nm); $\vec{E}_2$ is the polarization vector of the Nd^+-YAG laser (P_{GL} = 50 mW, λ_{GL} = 532 nm); $\vec{P}$ is the polarization direction of the polarizer; *M* is a plane mirror to redirect the Nd^+-YAG laser beam toward the sample. The screen in front of the sample contains a circular aperture at the center for laser passage and real-time observation of SAS patterns. The inset image shows a SAS pattern under irradiation by a He-Ne laser beam. The sample can rotate around the axis of the setup (i.e., *z*-axis). The angle *α* represents the angle between the two polarization vectors $\vec{E}_1$ and $\vec{E}_2$ on the surface of the sample

crisscrossing SPN with a different period and orientation (SPN2), a diode-pumped Nd^{+}-YAG laser ($P_{GL} = 50$ mW, $\lambda_{GL} = 532$ nm; second harmonic) were used as the incident beams.

As can be seen from Fig. 5, the second laser has to pass through a linear polarizer and then be reflected from a mirror to be redirected toward the sample; thus, at the end of its path, the power would be at the same order of magnitude as the first laser when arrives at the surface of the sample. These two exposures are successive, not simultaneous. It is known that at normal incidence, the period of the induced SPN (d) has a relation with the wavelength of the incident light (λ) as follows (Ageev and Miloslavsky 1995):

$$d = \frac{\lambda}{n_s} \tag{1}$$

where n_s is the index of refraction of the substrate. Therefore, the period of the SPN formed by the He-Ne laser beam equals to $d_R = \frac{\lambda_{RL}}{n_s} = \frac{632.8\text{nm}}{1.52} \approx 416\text{nm}$ and for the SPN formed by the Nd^{+}-YAG laser beam equals to $d_G = \frac{\lambda_{GL}}{n_s} = \frac{532\text{nm}}{1.52} \approx 350\text{nm}$. That is the formation of SPN with a shorter wavelength of the incident laser beam results in a smaller period for the produced grating. Because of that, we called the nanostructure made of these two C-SPNs: *bi-periodic*.

It should be noted again that for generating two C-SPNs at the same place, the irradiation of the sample should be carried out by two lasers on a fixed point of the sample, and it should be successive, not simultaneous. In this order, the two lasers have fixed vertical linear polarization, but the sample can rotate around the axis of the setup to be able to be irradiated successively with two different polarization orientations of incident beams at the same point on the sample (Fig. 5, α is the angle between the two orientations of polarization).

Small-angle scattering (SAS) and diffraction patterns

Upon irradiating the sample with a polarized laser beam, a pattern known as small angle scattering (SAS) emerges on the screen just before the sample (the inset of Figs. 5 and 6). The presence of this SAS pattern indicates the formation and development of the SPN. The time evolution of this SAS pattern is influenced by the PFB process, which we previously introduced in this article. Notably, the SAS pattern resembles two arcs intersecting at the vertex (as depicted in the inset of Fig. 5). For further details and explanations, please refer to Ref. (Ageev et al. 1997).

As a brief explanation for SAS patterns, the forming SPN has a domain structure (Figs. 2 and 3). Each grating domain (with index j) within the SPN corresponds to a vector, denoted as $\overrightarrow{K}_{D_j} = \frac{2\pi}{d} \bullet \hat{s_j}$, where $\hat{s_j}$ is the unit vector of the grating which is perpendicular to the grating's lines (or grooves) and d is the period of the grating. Each domain has some disorientation relative to the main vector of SPN with vector $\overrightarrow{K}$ (Fig. 2). The whole interaction area on the sample contains many domains within

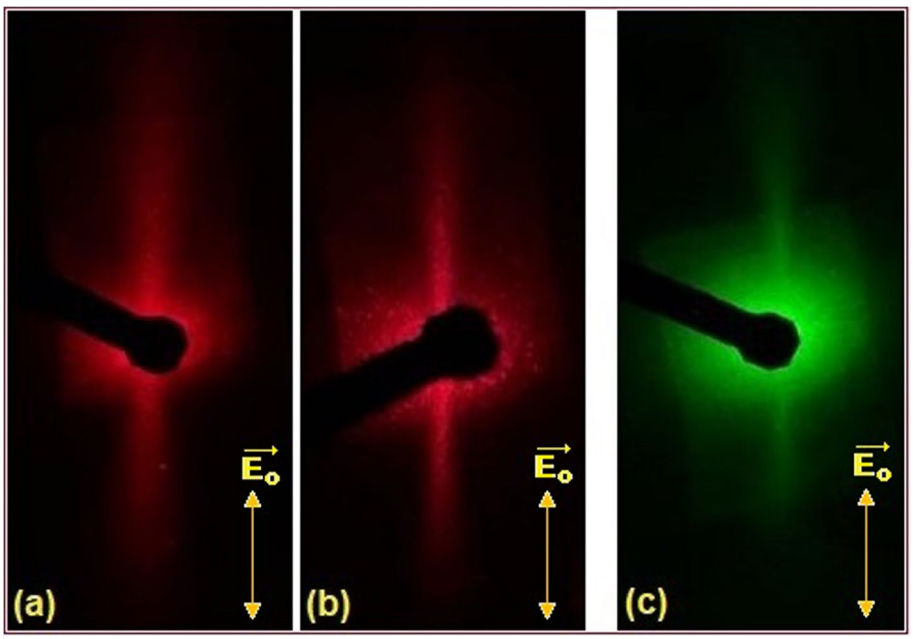

Fig. 6 SAS patterns from the samples: **a** after exposure to the He-Ne laser beam for 3 min; **b** after exposure to the He-Ne laser beam for 45 min; **c** after exposure to the Nd^{+}-YAG laser beam for 3 min. The inset (a') is the enlarged diffraction pattern of Fig. 6a

itself. Some borders of domains are highlighted on the SEM image shown in Fig. 2. To propagate along the forming SPN, an excited TE_n-mode with propagation vector $\vec{\beta}$ must satisfy the phase matching condition: $\vec{K} = \vec{\beta}$. Because of the domain structure of the generating SPN, while a mode is departing the border of the first domain ($\vec{K}_{D1}$) and enters into the next domain ($\vec{K}_{D2}$), scattering of the propagating mode happens. It should be remembered that $\vec{K}_{D1}$ and $\vec{K}_{D2}$ are not parallel. Consequently, some modes scatter from the interaction area on the sample and the SAS pattern appears on the screen (Ageev et al. 1997). SAS patterns from the samples of the present work are shown in Fig. 6. Figure 6a shows the SAS pattern from an SPN formed by a linear polarized He-Ne laser beam exposure for 3 min. Figure 6b displays the same pattern after 45 min of exposure, revealing the temporal evolution of the forming SPN, indicative of the role of the PFB process. Additionally, Fig. 6c presents the corresponding SAS pattern when the sample is exposed to a linearly polarized Nd^+-YAG laser beam for 3 min. The inset (a') of Fig. 6 provides an enlarged view of the diffraction pattern seen in Fig. 6a. Therefore, using the SAS pattern, one can determine whether the SPN formation is happening and assess the quality of the generated SPN.

Another tool for studying the formation of SPN is the diffraction pattern of the probe beam from the generated SPN (Nahal and Kashani 2017; Nahal et al. 1998; Miloslavsky et al. 1998; Miloslavsky et al. 1999; Nahal et al. 2019). As it was calculated in the "Sample preparation and the experimental setup" section, the period of the formed SPN is approximately 416 nm in the case of He-Ne laser irradiation, which is too small to allow for the observation of visible light diffraction from the SPN. To address this issue, researchers can employ a probe beam with a shorter wavelength, such as an N_2 laser (with a wavelength of $\lambda_{UV} = 337$ nm), to observe the diffraction pattern on the screen, located before the sample. Real-time observation of the diffraction patterns is not feasible due to the photosensitivity of the AgCl-Ag system and its relatively low diffraction efficiency [10, 18, and 24]. One layer of aluminum should be coated on the generated SPN to increase its diffraction efficiency [(Nahal et al. 1998), (Ageev et al. 1997), (Miloslavsky et al. 1998), (Miloslavsky et al. 1999), (Nahal et al. 2019), (Miloslavsky et al. 1998)]. To enable real-time observation of the diffraction pattern of forming SPNs, one can introduce a buffer layer between the AgCl layer and the substrate [(Nahal and Kashani 2017), (Miloslavsky et al. 1999), (Varminsky et al. 1998)].

In the case of double exposure of the samples with two laser beams with different directions of polarization and also different wavelengths (the present experiment), the diffraction pattern could be observed in real time without the buffer layer during the second exposure, as the wavelength of the incident beam in the second exposure is less than that of the first one (about 100 nm) (Fig. 7). The temporal evolution of SPN during the second exposure is apparent from the Fig. 7b, c. Diffraction of the second laser beam from the first grating is clear (Fig. 7b). Further exposure by the green laser leads to the formation of its corresponding grating, which in turn destroys the initial grating due to the limited availability of silver nanoparticles in the interaction area. Therefore, through the second exposure, the intensity of the diffraction pattern of the second laser from the first grating is reduced (Fig. 7c). The diffraction patterns have some spread appearance which is related to the formation of complex nanostructures and building blocks of the generating SPN and also the domain structure of the SPNs.

As illustrated in Fig. 7, for the second exposure which has a different wavelength and azimuth of polarization relative to the first one, we turn the sample around the axis of the setup, instead of rotating the lasers. To keep everything fixed in the setup, we use a mirror to lead the Nd^+-YAG laser beam toward the same spot on the sample which has been exposed, first, by the He-Ne laser beam (Fig. 5). Reflection from the mirror reduces the intensity of the Nd^+-YAG laser. Hence, its intensity would be comparable with the He-Ne laser beam intensity. In this way, any effect related to the difference in the intensities of the two interfering beams is reduced.

Schematically, Fig. 8 illustrates the outcome following the second exposure. Corresponding AFM image of SPN1 (Fig. 8a) and AFM image of bi-periodic criss-crossed SPN1+SPN2 with $\alpha = 45^\circ$ (Fig. 8b) are shown as insets of Fig. 8. The running TE_o mode of the AgCl slab waveguide exits from two sides of the sample (Fig. 8).

To summarize this section, upon irradiating a sample with a polarized laser beam, a SAS pattern appears, indicating the formation of the SPN. The SAS pattern evolves due to the positive feedback of the light (PFB) process. Scattering of TE modes at domain borders produces the SAS pattern. Real-time observation of diffraction patterns requires specific conditions, such as a buffer layer or double exposure with different laser beams (Nahal and Kashani 2017; Ageev et al. 2000).

AFM images of the samples

By analyzing AFM images, we quantified samples' average sizes and roughness containing bi-periodic self-organized plasmonic nanostructures (SPNs) formed at various angles (denoted by α). These measurements are presented in Fig. 9. Notably, after successive irradiation of the samples, the average size of the Ag-NPs increases (curve (a) of Fig. 9) relative to the average size of the Ag-NPs before the irradiation (~ 20 nm, line 1 in Fig. 9). The

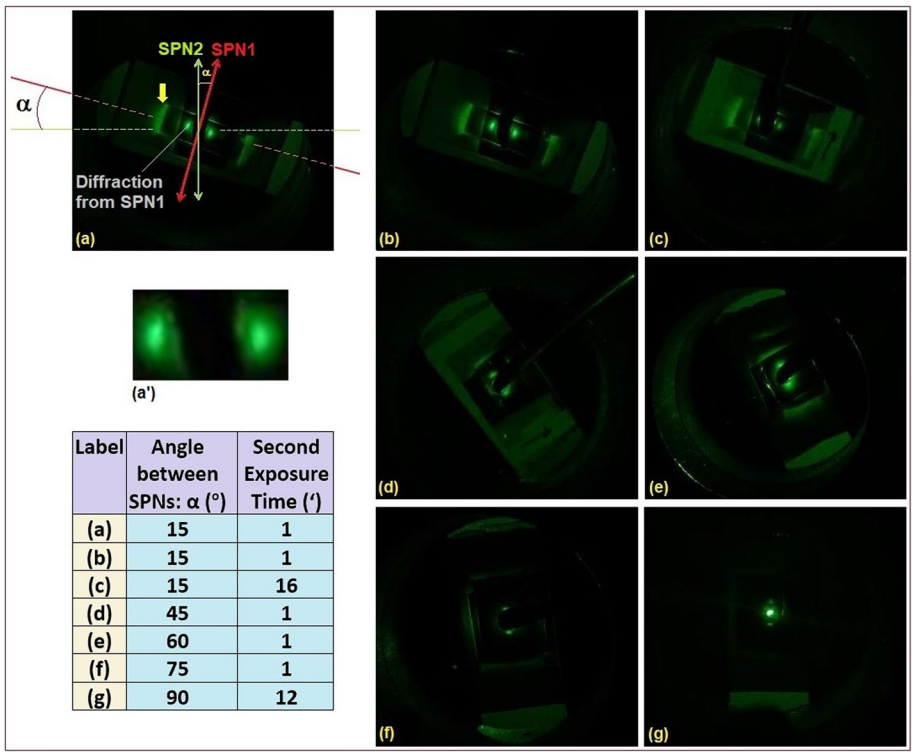

Label	Angle between SPNs: α (°)	Second Exposure Time (')
(a)	15	1
(b)	15	1
(c)	15	16
(d)	45	1
(e)	60	1
(f)	75	1
(g)	90	12

Fig. 7 **a** Diffraction patterns of Nd^{+}-YAG laser beam from the SPN1 (formed by the He-Ne laser beam during the first exposure). The Nd^{+}-YAG laser was used to generate the second SPN (SPN2) at the same place. The angle α is the angle between two polarization vectors $\vec{E}_1$ and $\vec{E}_2$ on the sample. The excited TE_0-mode of the AgCl slab waveguide which is exiting from two sides of the sample is marked by a yellow arrow; **b** the same as **a**; **c** diffraction pattern for the same angle $\alpha = 15°$, but with 16 min exposure time; **d**–**g** diffraction patterns for angle $\alpha = 45°$, 60°, 75°, and 90°, respectively, with 1 min exposure time. For $\alpha = 90°$, the exposure time was 12 min

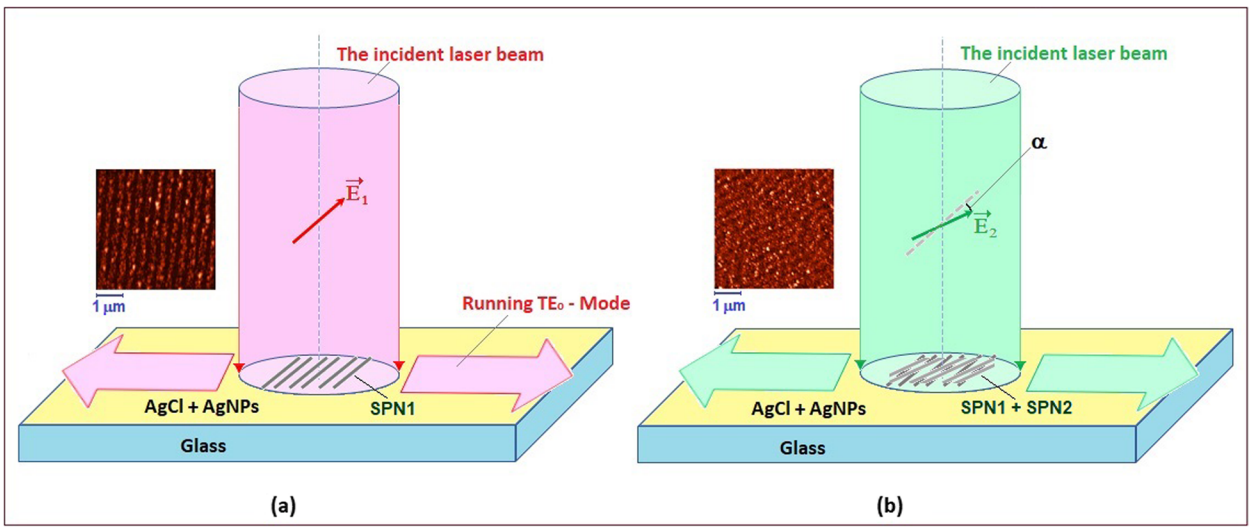

Fig. 8 Scheme for better understanding the data of Fig. 7. **a** Writing the SPN1 with He-Ne laser beam and **b** writing the SPN2 over the SPN1. Corresponding AFM images are shown as insets for each case

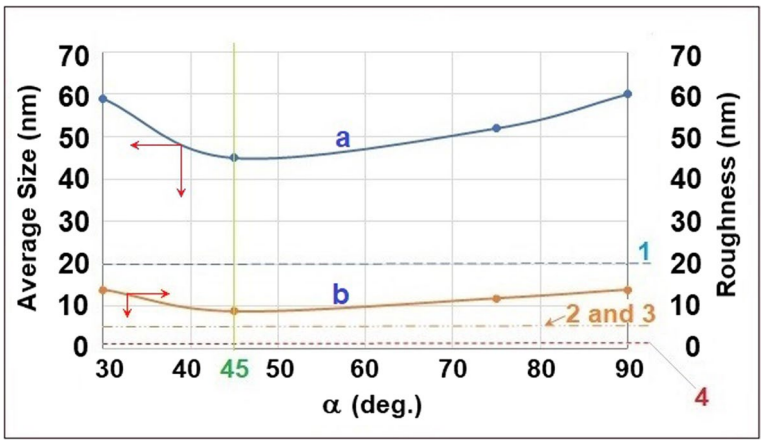

Fig. 9 **a** Average size of Ag-NPs; **b** the roughness of samples, as a function of angle α for the bi-periodic C-SPNs. Lines labeled with 1–4 are explained in the article

roughness of the samples also increases after the interaction (curve (b) of Fig. 9) relative to the roughness of non-irradiated samples (~ 5 nm, line 2 in Fig. 9). After the interaction, the average size of Ag-NPs and the roughness of the sample both reach their minimum values at $\alpha = 45°$ (Fig. 9). For comparison, the average size of Ag-NPs and the roughness of such island-like layer on a glass substrate (lines 3 and 4, respectively) are shown in Fig. 9. Examining the AFM images is important as they can be used to characterize the surface morphology of the samples. The surface morphology, in turn, influences the dissymmetry factor, subsequently impacting the samples' optical rotation power.

To better understand the difference between bi-periodic C-SPN and mono-periodic C-SPN structures and have some statistics about the surface morphologies of both C-SPN types, we took their AFM images and compared them (Fig. 10). Figure 10a shows AFM image of an SPN produced by a single linear polarized He-Ne laser beam ($\lambda_{RL} = 632.8$ nm). Figure 10b shows an AFM image of an SPN produced by a single linear polarized diode-pumped Nd^{+}-YAG laser beam ($\lambda_{GL} = 532$ nm. The exposure time for both cases was 30 min. In Fig. 10c, the AFM image of a mono-periodic C-SPN is shown, and in Fig. 10d, the AFM image of a bi-periodic C-SPN is shown. The exposure time for forming SPN1 was 20 min, and the formation of SPN2 was 10 min. For each AFM image, fast Fourier transformation (FFT) was calculated and is shown as top-right inset for each image. As can be seen from the FFTs of Fig. 10, in the case of bi-periodic C-SPN, the sample is more anisotropic relative to the mono-periodic one, which in turn boosts the chiroptical properties of the sample. In Fig. 11, enlarged AFM images of some of the complex chiral intersection points of bi-periodic samples (Fig. 10d) are shown. These chiral features have a high shape diversity. The enhancement of optical chirality with the increase of anisotropy will be explained later in the "Discussion" section of the article.

Some statistical studies of the samples using the AFM images of Fig. 10, with the help of the software NOVA, were conducted. The results are presented in Table 1. In Table 1, the surface skewness (*Rsk*) is a measure of the departure of the surface from symmetry. As can be seen for all cases in Fig. 10, we have $Rsk > 0$ which means the surface contains mainly peaks and asperities. The parameter Kurtosis (Sku) is a measure of the sharpness of the roughness profile. Sku > 3 means height distribution is spiked. In Table 1, for mono-periodic C-SPN, Sku is the maximum, but as our experimental data say, the bi-periodic C-SPN exhibit enhanced optical rotation. Thus, Sku has no meaningful influence on the enhancement. On the other hand, from Table 1, we can see that the bi-periodic sample has maximum roughness relative to other samples containing other types of SPN.

Spectroscopic studies (absorption, dichroism)

In Fig. 4c, absorption spectrum of the Ag/AgCl/Glass system is shown. There is an absorption peak around the wavelength $\lambda_{SPR} \approx$ 500 nm which is related to the red-shifted surface plasmon resonance (SPR) peak of Ag-NPs. A free Ag-NP has an SPR peak around $\lambda_{SPR}^{Free} \approx$ 410 nm (Kriebig and Vollmer 1995). However, it would undergo a red shift in the absorption spectrum due to the influence of the surrounding medium (AgCl Layer in our case) [(Kriebig and Vollmer 1995), (Jensen et al. 1999), and (Kresin 1995)]. Any variation in the size of the Ag-NPs also changes the position of the SPR peak in the absorption spectrum. A wide absorption peak indicates that we have a wide range size distribution of the Ag-NPs.

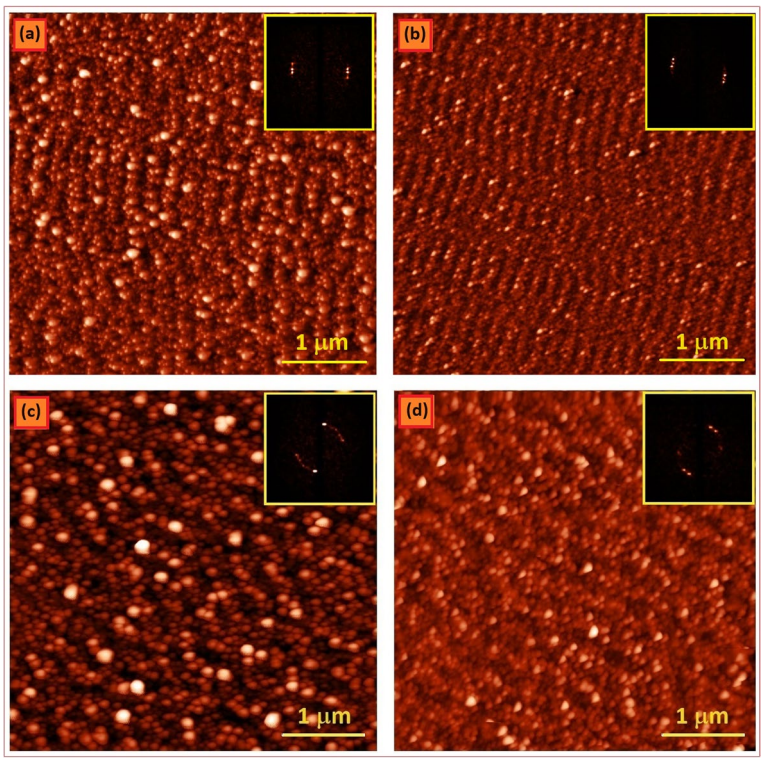

Fig. 10 AFM images of **a** single linear SPN formed by λ_R; **b** single linear SPN formed by λ_G; **c** mono-periodic C-SPN ($\lambda_R + \lambda_R$) with $\alpha = 45°$; **d** bi-periodic C-SPN ($\lambda_R + \lambda_G$) with $\alpha = 45°$. The FFT of each image is shown in the top-right inset

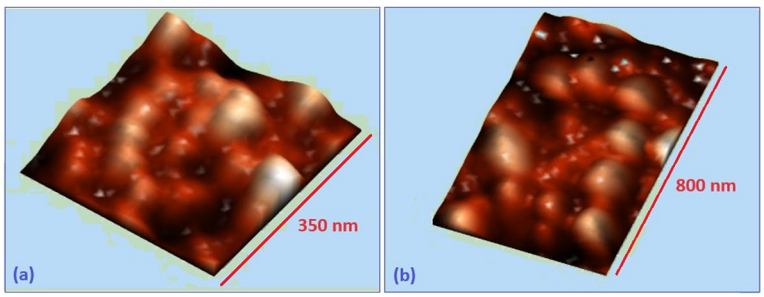

Fig. 11 Some enlarged parts of Fig. 10d. Intersection of SPN1 and SPN2 creates these chiral complex building blocks

Table 1 Surface morphology statistics based on AFM images of Fig. 10 about roughness, surface skewness (Rsk), surface kurtosis (Sku), and the average height of the samples' surfaces (Z)

SPN type	Roughness (nm)	Surface skewness - Rsk	Surface kurtosis - Sku	Average Z (nm)
Single linear SPN formed by λ_R	4.7	0.30	0.23	20.8
Single linear SPN formed by λ_G	10.8	1.02	1.80	45.0
Mono-periodic C-SPN ($\lambda_R + \lambda_R$)	8.3	1.80	4.00	31.5
Bi-periodic C-SPN ($\lambda_R + \lambda_G$)	23.9	0.94	1.53	105.0

Total exposure time: 30 min

To investigate any order or arrangement induced by the incident laser beam due to the formation of SPNs, one should measure the dichroism spectra of the irradiated samples. As a standard determination, dichroism means the difference in absorption for two linear polarized probe beams whose polarization vectors are perpendicular to each other [9, 10, 13, 16, and 24]. In this study, the term *dichroism* refers to the difference in absorption between two linearly polarized probe beams that are parallel to the self-organized plasmonic nanostructures (SPNs) generated by the He-Ne laser beam (SPN1, from the first exposure) and the SPN formed by the Nd^{+}-YAG laser beam (SPN2, from the second exposure). We considered the optical density, $D = -\log(T)$ where T is the transmittance of the sample, as a measure of attenuation (absorption + scattering). If $D_R^{||}$ represents the optical density for the SPN1 and $D_G^{||}$ represents the optical density for the SPN2, then we introduce $\Delta D_{RG} = D_R^{||} - D_G^{||}$ as the *dichroism* for our samples. By the upper index "||", we mean the polarization vector of the probe beam, $\vec{E}_p$, was parallel to $\vec{E}_o$ which is the polarization vector of the writing laser beam. For example, we have measured the dichroism for the samples that contain bi-periodic SPNs with different angles, α for a probe beam light with wavelength $\lambda_R = 625$nm (Fig. 12). From Fig. 12, we can see that for $\alpha = 45°$, the sign of dichroism is negative. It means that for a bi-periodic SPN system generated with $\alpha = 45°$, we have $D_R^{||} < D_G^{||}$. In general, the formation of SPN2 over the SPN1 increases the disorder of the complex nanostructure. This is obvious because the SPN2 needs Ag-NPs for its formation and takes them from already existing SPN1, due to the limitation in the number of available silver nanoparticles in the interaction area on the sample. The existence of dichroism for a sample indicates that there is an order and arrangement of Ag-NPs over it, i.e., the SPNs. It is well-established that dichroism affects the dissymmetry factor of the nanostructure, which subsequently governs the optical rotatory power of the samples (Nahal and Talebi 2014; Nahal and Kashani 2017).

To study the impact of chiral building block morphology on the induced optical activity of bi-periodic C-SPNs, we need to measure the circular dichroism of the samples. Circular dichroism quantifies the difference in absorption between right-handed and left-handed circularly polarized probe beams. The circular dichroism equals CD = D_R - D_L, where the optical density equals $D_j = -\log T_j; j = R\text{or}L$ stands for right-handed or left-handed circular polarized probe beams, respectively. $T_j = \frac{I_j}{I_0}$ is the transmittance of right- or left-handed probe beams. The parameter I_j is the intensity of the probe beam after the sample, and I_o is the intensity of the probe beam without the sample. Using CD, one could determine the dissymmetry factor. The dissymmetry factor $g = \frac{CD}{\frac{1}{2}(T_R - T_L)}$ is a factor that represents the influence of the geometry and morphology of the formed complex Ag-NPs (Barron 2004; Nahal and Talebi 2014; Nahal and Kashani 2017). The result is shown in Fig. 13. This measurement is performed for $\lambda_R = 625$nm. From Fig. 13, we can conclude that in general, the dissymmetry factor for the case of bi-periodic C-SPNs is higher than that of mono-periodic ones. At angle $\alpha = 45°$, the factor g reached its maximum value. This is the angle at which the dichroism has a negative sign (Fig. 12).

To summarize this section, spectroscopic studies show that after the formation of bi-periodic C-SPNs, the dissymmetry increases relative to the case of mono-periodic C-SPNs which confirm an increase in anisotropy of the

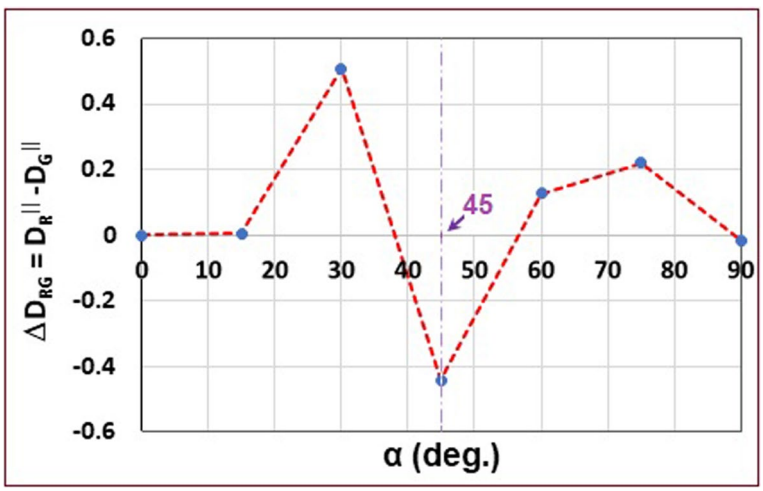

Fig. 12 Variation of the induced dichroism with angle *α* for bi-periodic C-SPNs

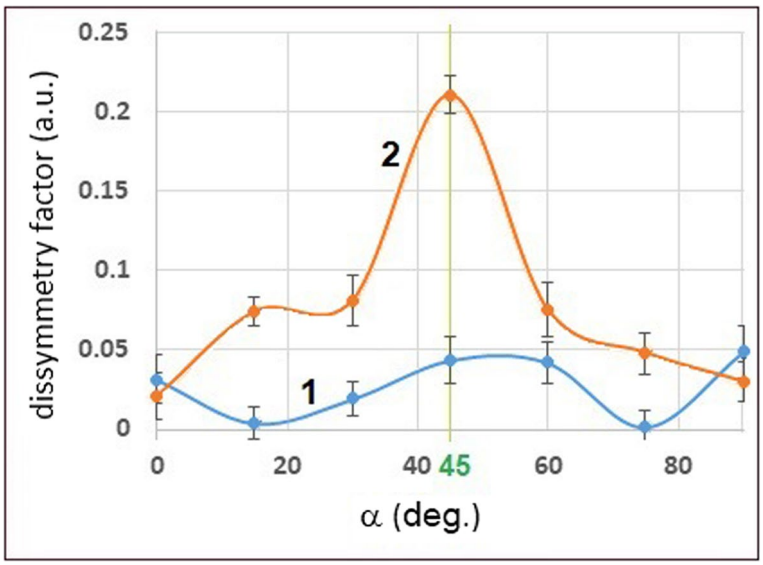

Fig. 13 Dissymmetry factor vs. angle α for (1) mono-periodic C-SPNs and (2) bi-periodic C-SPNs. For bi-periodic C-SPNs, the dissymmetry factor reaches its maximum value at $\alpha = 45^{\circ}$

samples by bi-periodicity enhances the optical rotation power of the samples.

Optical rotation measurements

For measuring the amount and sign of optical rotation angle ($\boldsymbol{\theta}$) of the polarization plane of the linear polarized probe beam $\vec{E}_p$, the setup shown in Fig. 14 was set and used. A linear polarized probe beam (it was a tunable LED with wavelengths: $\lambda_B = 465$nm, $\lambda_G = 525$nm, $\lambda_Y = 590$nm, and $\lambda_R = 625$nm) was used as the source. After the source, a Nicole prism was placed as a polarizer to make the probe beam linear polarized light. Next, the second Nicol prism (i.e., analyzer) should be oriented perpendicular to the polarization direction of the polarizer. This arrangement ensures that the detector, positioned immediately after the analyzer, receives a

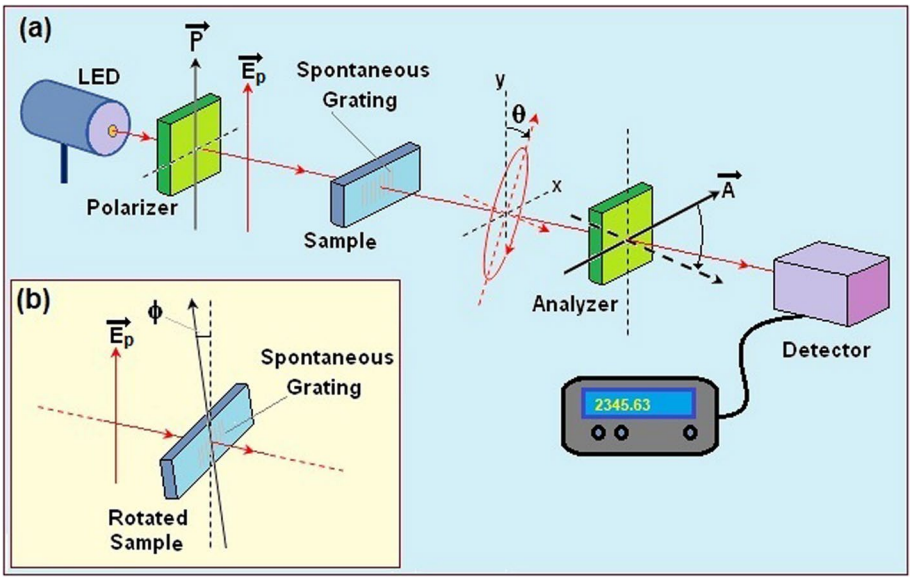

Fig. 14 Experimental setup for optical rotation measurement. The LED plays the role of a light source. $\vec{E}_p$ represents the polarization vector of the probe beam. $\vec{P}$ is the polarization direction of the polarizer. $\vec{A}$ is the polarization direction of the analyzer. θ is the angle of induced optical rotation. φ is the angle of the vertical axis of the sample relative to the $\vec{E}_p$

minimal signal (i.e., the zero point of the setup). When an optically active sample is placed between the polarizer and the analyzer (as shown in Fig. 14), the signal detected is no longer at its minimum. As the probe beam passes through the sample, its plane of polarization undergoes rotation, causing it to deviate from the perpendicular alignment with the analyzer. To restore the minimum signal, the analyzer must be rotated by an angle equal to the rotation of the probe beam's polarization plane (denoted as $\boldsymbol{\theta}$). The probe beam in addition to the rotation of its polarization plane, becomes an elliptical polarized light which is related to the induced anisotropy in the samples (Nahal and Kashani 2017).

There is a standard method for measuring the optical activity of a medium and determining the portion of induced anisotropy and chirality, separately (Kuwata-Gonokami et al. 2005; Nahal and Kashani 2017; Nahal et al. 2019). In this method, at first, the angle $\boldsymbol{\theta}$ is measured. Then, the measurement is conducted for different orientations of the sample relative to the polarization vector of the incident laser beam ($\vec{E}_o$) at the first exposure (called an angle ϕ) (Fig. 14). We measured the optical rotation for both cases: (i) mono-periodic C-SPNs and (ii) bi-periodic C-SPNs. As an example, the results of such measurement with a red probe beam ($\lambda_R = 625\text{nm}$) are shown in Fig. 15. This measurement is performed for case (ii) when $0° \leq \alpha \leq 90°$ with an interval equal to $\Delta\alpha = 15°$, at the range of $-90° \leq \phi \leq +90°$. At first glance, it may seem that no specific relationship exists between angle α and induced chirality and anisotropy values. But, Fig. 15 shows that the variation of angle $\boldsymbol{\theta}$ vs. angle ϕ has a sinusoidal behavior for all values of angle α. We should fit an appropriate curve to this experimental data. In this order, we used a general function as follows (Svirko and Zheludev 1998; Tanaka et al. 2012):

$$\theta = A\sin[2(\phi - B)] + C \tag{2}$$

where B and C enter an offset (usually $C << B$). By definition, the fitted curve's offset amount shows the degree of chirality, and the maximum of the amplitude A represents the measure of the anisotropy of the medium.

Based on the abovementioned method, the variation of the maximum angle of rotation for the red probe beam ($\boldsymbol{\theta}_{max}$) with angle α (Fig. 16a) and also the variation of the amount of optical rotation due to induced chirality (γ) with the angle α (Fig. 16b) are measured, for both cases (i) and (ii). Our results indicate that the induced optical rotation is enhanced, in general, for the case of bi-periodic C-SPNs (Fig. 16a, curve 1) in comparison with the case of mono-periodic C-SPNs (Fig. 16a, curve 2). It is also obvious from Fig.16a that the general trend of variation of $\boldsymbol{\theta}_{max}$ vs. angle α is decreasing with the increase of angle α, for both cases (i) and (ii) (Fig. 16a: lines 1' and 2', respectively). Meanwhile, for the case of bi-periodic C-SPNs average of the maximum angle of rotation ($\boldsymbol{\theta}^{RG}{}_{max} = 4.7°$) is larger than that of the case of mono-periodic C-SPNs ($\boldsymbol{\theta}^{RR}{}_{max} = 3.6°$). Its trend line (line 1' in Fig. 16a) stands about 30% higher than that of the case of mono-periodic SPN (line 2' in Fig. 16a). Hence, bi-periodicity can be considered as an enhancement factor for the induced optical activity, for our samples.

In Fig. 16b, the measured variation of the angle of rotation due to the induced optical chirality (γ) with the angle α is shown. Curve 1 of Fig. 16b is the variation of γ with α for bi-periodic C-SPNs, and curve 2 is the variation of γ with α for the mono-periodic ones. As it can be seen, in general, we have $\gamma^{RG}_{Ave.} = 2.4° > \gamma^{RR}_{Ave.} = 1.7°$, where $\gamma^{RR}_{Ave.}$ is the average angle of rotation due to the induced optical chirality for mono-periodic C-SPNs (line 1' in Fig. 16b) and $\gamma^{RG}_{Ave.}$ is the average angle of rotation due to

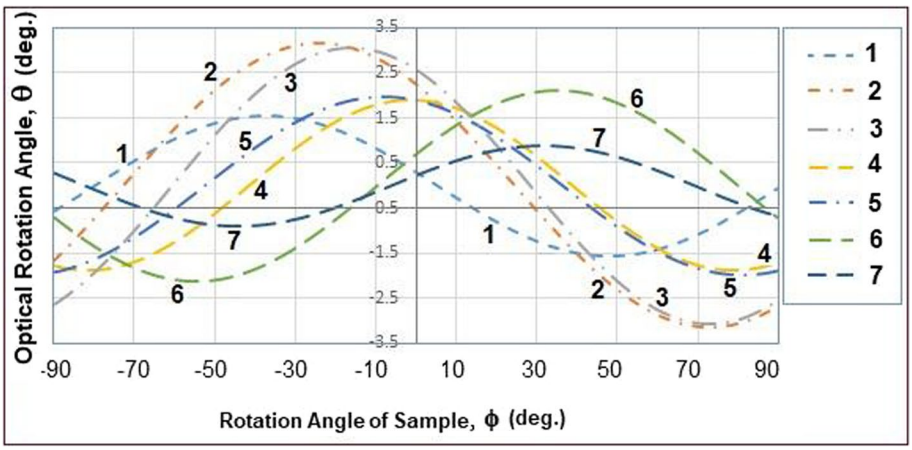

Fig. 15 Variation of optical rotation angle θ vs. angle φ for different angle α. Curves 1–7 represent the abovementioned variation for $\alpha = 0°$, 15°, 30°, 45°, 60°, 75°, and 90°, respectively

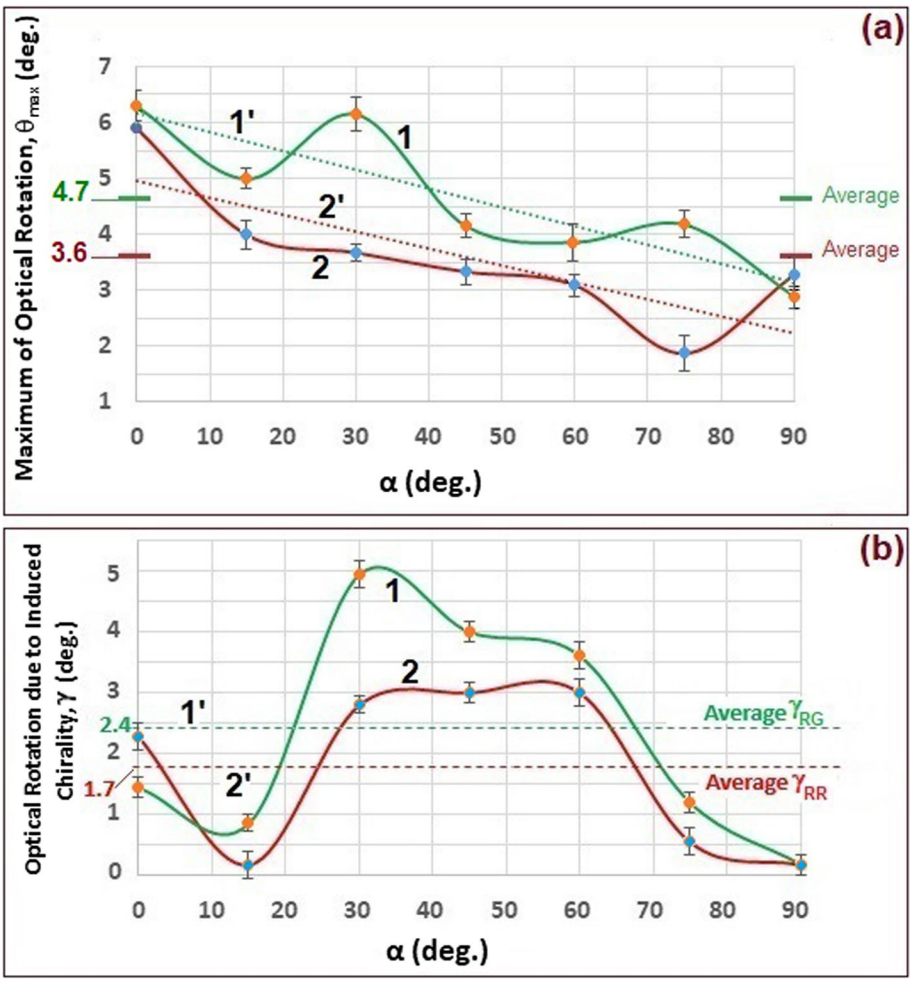

Fig. 16 **a** Maximum optical rotation vs. angle *α* for bi-periodic C-SPNs (curve 1) and mono-periodic C-SPNs (curve 2). The average angle *θ* is determined for both cases and written on the vertical axis. Dotted lines represent the trend of each case. **b** The optical rotation due to the chirality (*γ*) vs. angle *α* for both cases: bi-periodic C-SPNs (curve 1) and for mono-periodic ones (curve 2). Average *γ* is measured and shown for each case (lines 1′ and 2′, respectively)

the induced optical chirality for bi-periodic C-SPNs (line 2' in Fig. 16b). That is, the *bi-periodicity* increases the induced optical chirality by approximately 41%, which is a remarkable result.

To investigate the relation between the wavelength of the probe beam and the optical rotation of the samples, we measured the optical rotation of a sample with $\alpha = 45°$ for different angles ϕ for the following wavelengths: $\lambda_B = 465$ nm; $\lambda_G = 525$ nm; $\lambda_Y = 590$ nm, and $\lambda_R = 625$ nm . The results are shown in Fig. 17a. As it can be seen, in general, the longer wavelength rotates more than the shorter one. Figure 17a also indicates that the probe beam with a wavelength of $\lambda_G = 525$ nm which closely aligns with the surface plasmon resonance (SPR) peak at $\lambda_{SPR} \sim 500$ nm, exhibits maximum rotation. We can also see that the probe beam with $\lambda_B = 465$ nm has the minimum rotation and has the opposite sign of rotation relative to the three other probe beams. In Fig. 17b, variation of the maximum optical rotation versus the wavelength of the probe beam is plotted. These data indicate that there is an optical rotatory dispersion for bi-periodic C-SPNs, and there is an anomaly in the vicinity of the SPR peak. That is, for the blue probe beam, the sign of optical rotation differs from the rest of the probe wavelengths, which are longer than that of the SPR peak.

Ellipsometry

According to previous studies (Nahal and Talebi 2014; Nahal and Kashani 2017; Nahal et al. 2019), we know that when a probe beam passes through our optically active sample, an ellipticity is induced in addition to the induced optical rotation of the polarization vector of the probe beam. It has been demonstrated that the induced

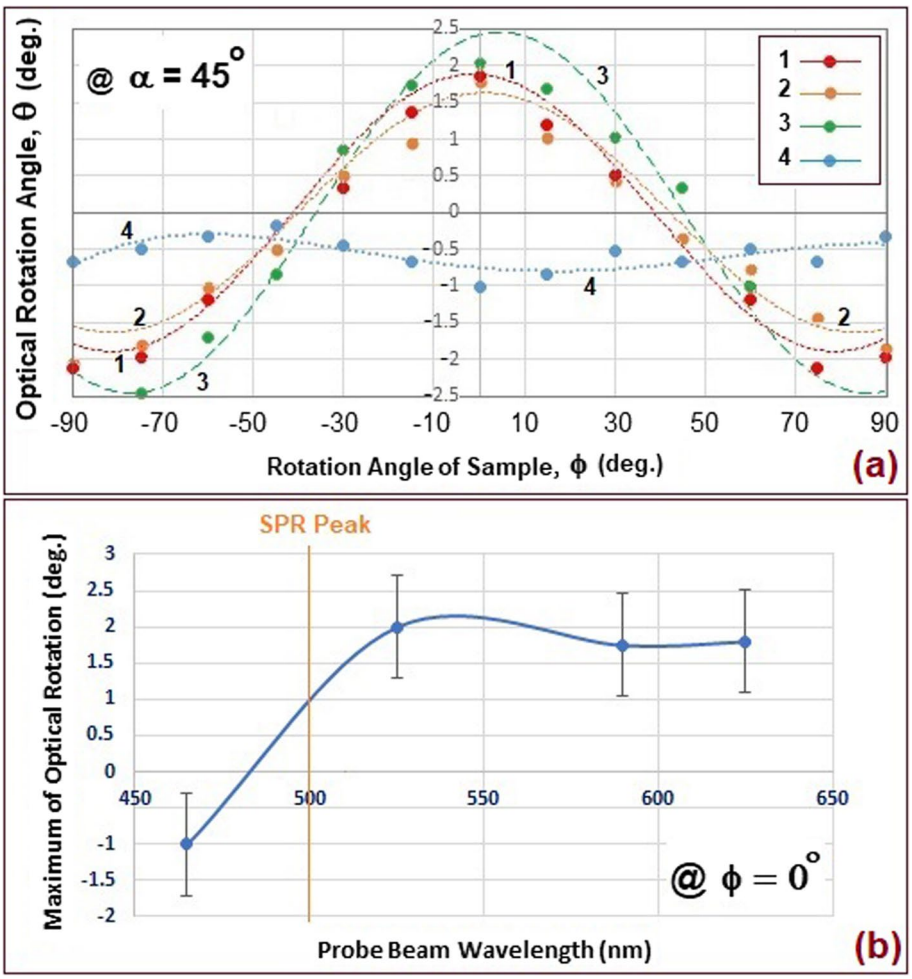

Fig. 17 **a** Dependence of optical rotation angle to the wavelength of the probe beam at $\alpha = 45°$; **b** Optical rotation dispersion of θ_{max} relative to the SPR absorption peak (~ 500 nm) at $\varphi = 0°$

ellipticity is related to the anisotropy of the sample containing C-SPNs (Nahal and Kashani 2017).

To study the polarization ellipse of the probe beam after the samples, we first pass the probe beam through a linear polarizer. Then, after the polarizer, we put the sample and after that an analyzer which is parallel to the polarizer. At the end of the setup, we measure the intensity of the probe beam. If we repeat this measurement every 5° of rotation of the analyzer and plot a polar diagram, we will obtain a *figure-8-like* diagram (Fig. 18). The azimuth of this diagram represents the azimuth of the polarization ellipse of the probe beam. The arctangent of the ratio of the smallest diameter (diameter*a*) to the largest one (diameter*b*) equals to: $\chi = \arctan(\frac{a}{b})$, which is called ellipticity (Fig. 18c). The angle of the azimuth of this polar diagram equals the angle of optical rotation of the probe beam (Fig. 18a) (https://laser.physics.sunysb.edu/kristine/report/index.html.). From this measurement, we observed that for the sample including a bi-periodic C-SPN, the maximum rotation for the probe beam obtains about ~ ±7° at an angle $\alpha = \pm 60°$. The amount of rotation observed in this sub-wavelength optical active nanostructure is notable. The sample's structure consists of an AgCl layer on a glass substrate and coated by an Ag-NPs thin film, with a combined thickness of approximately 65 nm.

We also measured the ellipticity of the probe beam for both cases: mono-periodic and bi-periodic SPNs with different angles α (Fig. 18b). We observed, for mono-periodic SPNs, maximum of ellipticity obtained at $\alpha = 30^{\circ}$, and for bi-periodic ones, it happens at $\alpha = 15^{\circ}$. Results of Fig. 18b also confirm that the ellipticity of the probe beam, which is directly related to the anisotropy of the samples (Nahal and Kashani 2017), is generally higher for bi-periodic C-SPNs relative to the mono-periodic ones (~ 34% on average).

Comparing these results with the results presented in Fig. 16 brings us to the conclusion that the induced

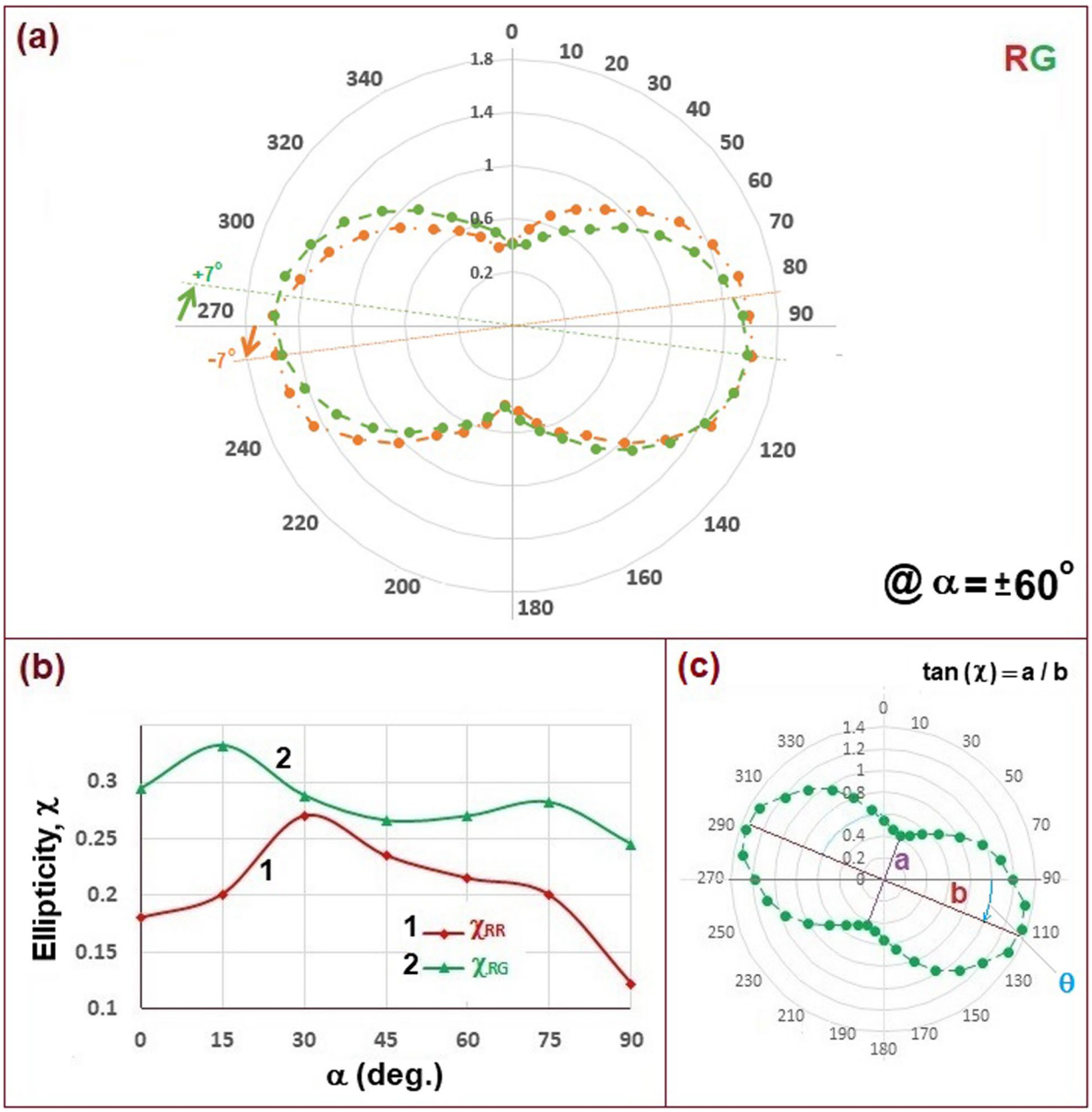

Fig. 18 **a** Polar diagram of the measured ellipse of polarization of the probe beam after the sample with $a = +60°$ (the green diagram with azimuth of +7°) and $a = -60°$ (the orange diagram with azimuth of −7°). The azimuth angle of the probe beam ($\vec{E}_p$) before the samples was in line with angle 270° of the polar diagram; **b** Change of ellipticity of the probe beam (χ) for a different angle a for mono-periodic C-SPNs (curve 1) and bi-periodic ones (curve 2); **c** Schematic polar diagram to show how the ellipticity and azimuth angle of the probe beam are determined and measured

anisotropy in the samples, due to the formation of complex C-SPNs, is a crucial parameter causing the optical rotation and enhances the induced optical chirality. Results presented in Fig. 18a also show that the complex nanostructure that was formed has recorded the information about the sign of rotation of SPN2 relative to the SPN1 (i.e., sign of rotation of sample around the setup axes.)

Discussion

As it was explained in the "Introduction" section, an interference pattern forms on the sample's surface when a polarized laser beam interacts with a photosensitive slab waveguide thin film (AgCl) coated with Ag nanoparticles. The Ag nanoparticles migrate to the interference pattern's minima, creating a self-organized periodic nanostructure (SPN). This nanostructure encodes information about the incident light's wavelength, polarization state, angle of incidence, and substrate's refractive index (in our case, glass: $n_s = 1.52$).

Previous research has demonstrated that AgCl-Ag thin films with intricate SPNs can rotate the plane of polarization of a linearly polarized probe beam (Nahal and Talebi 2014; Nahal and Kashani 2017; Nahal et al. 1998; Nahal et al. 2019). In other words, after the interaction, these films exhibit optical activity. This optical activity arises from two factors: (1) anisotropy of the formed SPN and (2) optical chirality induced in the sample due to the complex SPN formation. These films exhibit fascinating optical behavior, influenced by their nanostructure and chirality.

It is shown (Nahal and Talebi 2014; Nahal and Kashani 2017) that the increase in anisotropy of the sample could significantly enhance the optical rotation power due to the existence of optical chiral building blocks of the complex SPNs (Murai et al. 2011; Nahal and Talebi 2014; Fan and Govorov 2010). Bi-periodic C-SPN has a more dissymmetric structure relative to the mono-periodic C-SPN (Fig. 13), as the period of SPN2 differs from the period of SPN1. This is because their period depends on the wavelength of the writing laser beam (relation (1)). In other words, bi-periodicity introduces preferred directions in the medium and formation of complex anisotropic nanoparticles, most of which have chiroptical properties.

Anisotropic complex chiral nanoparticles formed at intersection points of SPN1 and SPN2 (Figs. 11 and 19) exhibit different interactions with left- and right-handed circularly polarized probe light. This differential interaction leads to stronger circular dichroism which is a sign of chiroptical activity. It is called *enhanced circular dichroism* (recent advances in their synthesis and applications 2022). On the other hand, anisotropic shapes can support localized surface plasmon resonances more effectively than isotropic shapes (localized surface plasmon resonance). These resonances amplify the electromagnetic fields at the nanoparticle surface, enhancing the interaction with polarized probe light and therefore boosting chiroptical effects (Li et al. 2022). If the complex chiral building blocks as a dipole are considered, with an anisotropic shape, then during the interaction with the polarized probe beam, these dipoles interact differently with vertical and horizontal polarized probe lights, leading to enhanced optical activity (Fig. 20). The intersection points of SPN1 and SPN2 could be considered as anisotropic nanoparticles assembled into larger chiral structures, which exhibit even stronger chiroptical effects. These assemblies can create complex interactions with light, leading to

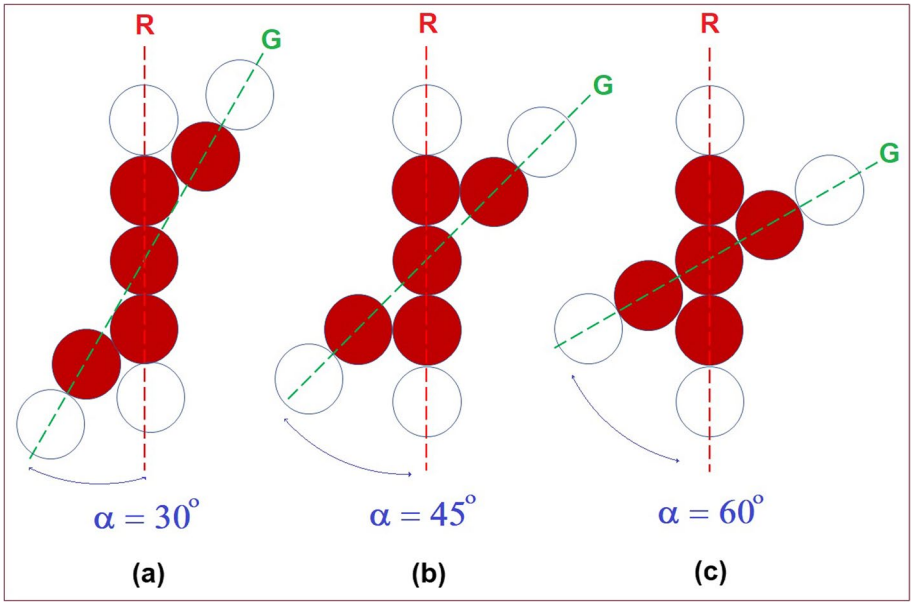

Fig. 19 Schematic drawing to show what possible variants of the chiral building blocks could be formed at different angles *a* at crisscrossing points of SPN1 and SPN2

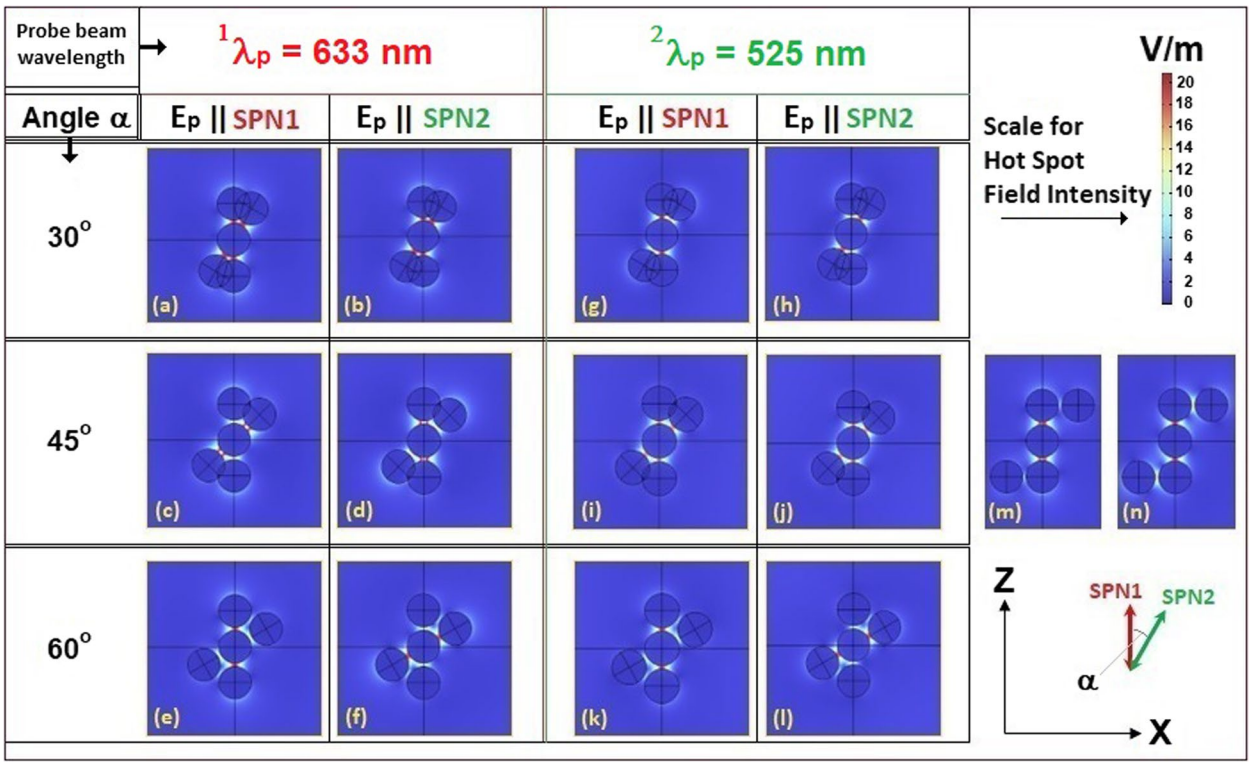

Fig. 20 Calculated electrical field distribution of the interacting linear polarized probe beam (with polarization vector lying at *Z-X* plane and propagating along the *y*-axis) for different directions of $\vec{E}_p$ around the Ag-NPs chains at crossing points of SPN1 and SPN2. These calculations are performed for two different wavelengths of the probe beams: figures **a**–**f** for $^1\lambda_p$ = 633 nm and figures **g**–**l** for $^2\lambda_p$ = 525 nm. The calculations also were performed for a different angle *α*: figures **a**, **b**, **g**, and **h** for $\alpha = 30°$; figures **c**, **d**, **i**, and **j** for $\alpha = 45°$; figures **e**, **f**, **k**, and **l** for $\alpha = 60°$. Figures **m** and **n** are calculated for $\alpha = 45°$ and $^1\lambda_p$ = 633 nm but with larger gaps between Ag-NPs of the SPN2 chain

enhanced optical activity. In conclusion, the increase in anisotropy, using bi-periodicity, enhances the chiroptical properties of our samples, containing complex chiral structures, by amplifying interactions with polarized probe light, supporting strong plasmon resonances.

In the context of rotating the plane of polarization in AgCl-Ag thin films, there exist several methods to achieve this effect: (i) irradiating the samples with elliptically or circularly polarized incident light (Nahal and Talebi 2014; Nahal et al. 1998), (ii) off-normal incidence of the laser beam (Hirbodvash et al. 2015), (iii) generation of two identical crisscrossed linear SPNs (*mono-periodic SPNs*) with different angles between the two SPNs (named angle α) (Nahal and Kashani 2017), and (iv) simultaneous excitation of TE_0 and TE_1 modes of thick photosensitive layers (Nahal et al. 2019). In case (i), the degree of ellipticity of the elliptically polarized incident light controls the sign and amount of optical rotation. In case (ii), the incident angle can play the role of the control parameter for the sign and amount of optical rotation of the probe beam. In case (iii), the parameter control is the angle between the two crisscrossed gratings (i.e., angle α), and in case (iv), the thickness of the layer plays the role of the control parameter.

Following our abovementioned research, to enhance the induced optical activity in such thin films, we examined the *bi-periodicity* of a complex nanostructure as a candidate parameter for enhancing the induced optical rotation. Our experimental data confirmed that producing the bi-periodic C-SPNs has the highest optical rotation power among the aforementioned methods.

From the SAS patterns of the forming SPN shown in Figs. 6a, b, one spots the temporal evolution of the forming nanostructure. As was mentioned in the "Small-angle scattering (SAS) and Diffraction patterns" section, the appearance of the SAS pattern indicates that the SPN is forming, and the comparison of Figs. 6a, b shows that the PFB mechanism, discussed in the "Sample preparation and the experimental setup" section, is functioning. Thus, we should find the optimum exposure times to achieve the best quality for the C-SPNs. We learned that 20 min of exposure for the formation of SPN1 (irradiation by He-Ne laser beam) and 10 min of exposure for the formation of SPN2 (Nd^+-YAG laser beam; second harmonic) results in the best achievable bi-periodic C-SPNs. During

the second exposure, we can observe (in real-time) the diffraction pattern of the second incident laser beam from the already existing SPN1 (Fig. 7). It could happen because the second laser has a shorter wavelength of approximately 100 nm compared to the first laser. Therefore, its diffraction could be observed on the surface of the samples during the interaction. That is, the AgCl layer acts as a buffer layer, letting us observe the diffraction pattern from the existing and forming C-SPNs in real-time, for monitoring the entire process. This method enables us to achieve optimal results (Nahal and Kashani 2017; Nahal et al. 1998).

It can be seen from Fig. 16a that with the increase of angle α, the maximum angle of rotation $\boldsymbol{\theta}_{\max}$ has a decreasing trend for both mono-periodic and bi-periodic C-SPNs. That is an increase of angle α results in decreasing the anisotropy of the samples. But, in general, the bi-periodicity has increased the optical rotation of samples by an average of 30% (Fig. 16a). On the other hand, for angle α between 30° and 75°, the induced optical chirality reaches its maximum values (Fig. 16b), which means more complex assemblies made of Ag-NPs are created.

In Fig. 18b, the variation of ellipticity of the probe beam after the sample (χ) versus angle α is plotted. The bi-periodicity has enhanced the quantity χ by an average of 40%. It is known that (Nahal and Kashani 2017) the quantity χ is a measure of induced anisotropy, which in turn boosts the induced optical chirality. That is, the induced bi-periodicity increases the anisotropy of the irradiated samples. These data are consistent with the data presented in Fig. 16.

Figure 17 shows that for a certain angle α (for this plot it was $\alpha = 45°$), the maximum amount of rotation of the probe beam is a function of the wavelength of the probe beam. Figure 17b shows that for the probe beam with a wavelength smaller than that of the surface plasmon resonance (SPR) peak of Ag-NPs (used for the construction of C-SPNs), the sign of optical rotation is in the opposite direction of those of probe beams with wavelength longer than that of SPR peak. It seems that there is an *optical rotatory dispersion* in the vicinity of the absorption peak of the SPR spectrum. It is very similar to the case of the rotatory strength behavior of molecules in the vicinity of absorption bands. In the case of a molecule, the angle of rotation of the probe beam for a dispersive medium is given as (Atkins and Friedman 2005):

$$\Delta\theta \approx \frac{Nl\mu_o\omega^2 R_{k0}}{3\hbar\left(\omega_{k0}^2 - \omega^2\right)} \tag{3}$$

where N is the number of molecules, l is the length of the medium, μ_o is the vacuum permeability, R_{k0} is the rotational strength, ω_{k0} is the frequency of the absorption peak, and ω is the frequency of the probe beam. For the blue probe beam, we have $\omega_{k0}^2 - \omega^2 < 0$, then $\Delta\theta$ becomes negative, that is, the blue probe beam rotates in the opposite direction relative to the probe beams of longer wavelength for which $\omega_{k0}^2 - \omega^2 > 0$. The optical rotatory dispersion for the samples confirms that the morphology of the induced chiroptical building blocks of the complex SPNs plays an essential role in inducing optical activity in such photosensitive thin film systems *(Ag/AgCl/glass* system in our case).

As mentioned earlier, absorption spectroscopy using linearly polarized probe beams allows us to examine the induced dichroism resulting from the formation of C-SPNs. The data presented in Fig. 12 indicate that the angle α between the two C-SPNs influences the amount and sign of induced dichroism which is related to the morphology of the crossing points of SPN1 and SPN2. But as it can be seen from Fig. 12 for $\alpha = 45^{\circ}$, the sign of dichroism is negative, and for the same α, the dissymmetry factor (Fig. 13) reaches its maximum value. It should be related to the geometrical properties of these complex structures and their chiral crossing points. A change in angle α changes the shape of chiral building blocks which may be created in crossing points of the two gratings (Fig. 19). The number of available Ag-NPs for generating the chiral units is also an important factor.

Results of our calculations indicate that the fill factor (FF) which is the abundance of Ag-NPs on the surface of the samples would not be changed dramatically for different bi-periodic C-SPNs with different angles α. For the non-irradiated sample, we have FF = 61%, but the average fill factor for all C-SPNs with a different angle α is about $\mathrm{FF}_{\mathrm{Ave.}} \sim 47.5\%$. This implies that the fill factor cannot be considered as a major parameter for optical rotation enhancement for our samples and has no deterministic and clear relation to the angle α.

To understand the dramatic change of sign of dichroism at $\alpha = 45^{\circ}$, we investigated the electrical field distributions around the Ag-NPs, known as hot spots, which have participated in creating the chiral units in the crossing points of C-SPNs during the interaction. We used COMSOL software for the simulation of electrical field distribution around the crisscrossed Ag-NPs chains (Fig. 20). The calculation was performed for two probe beams with different wavelengths ($^1\lambda_p$ = 633 nm and $^2\lambda_p$ = 525 nm). We limited ourselves only to three angles: $\alpha = 30^{\circ}, 45^{\circ}$, and 60°. For each λ_p, we considered two cases: (1) when the polarization vector of the probe beam ($\vec{E}_p$) was parallel to the grating lines of SPN1 (Fig. 20a, c, e, g, I, k) and (2) when the vector $\vec{E}_p$ was parallel to the grating lines of SPN2 (Fig. 20b, d, f, h, j, l). As it can be seen for $\alpha = 30^{\circ}$, Ag-NPs of each SPN's lines are connected. Also, there is a small gap (about 10 nm)

between the Ag-NPs of each chain. Thus, the hot spots have occurred only along the chains of each SPN at the gaps between the Ag-NPs. It is well established that if the polarization vector of the probe beam ($\vec{E}_p$) is parallel to a chain of Ag-NPs ($\vec{E}_p \vec{E}_o$), the maximum absorption will happen (Nahal and Talebi 2014; Nahal and Kashani 2017; Nahal et al. 2019), and for the case when $\vec{E}_p \perp \vec{E}_o$, the minimum value of absorption obtains. From the simulation presented in Fig. 20, we can see that for all angle α, except $\alpha = 45^\circ$, for the chains parallel to $\vec{E}_p$, stronger hotspots are generated along it, relative to the chains which line with $\vec{E}_p$. As illustrated in Fig. 20a, b, g, h, for the case $\alpha = 30^\circ$, the Ag-NPs near the crossing points of the two SPNs overlap each other, decreasing the difference in intensity of the hotspots of the two crossing chains. For the probe beam with a shorter wavelength ($^2\lambda_p = 525$nm), this difference is clearer. As depicted, for angle $\alpha = 45^\circ$ the situation is reversed, i.e., along the direction of $\vec{E}_p$ hotspots are weaker (Fig. 20c, d, I, j). A weaker hotspot means less absorption for the linear polarized probe beam. This result justifies the data presented in Fig. 12. As shown in Fig. 12, for $\alpha = 45^\circ$, the dichroism is negative. That is, absorption along the chains of SPN parallel to $\vec{E}_p$ is less than that of other SPNs which is unparalleled to $\vec{E}_p$ leading to negative ΔD_{RG}, where $\Delta D_{RG} = D_R^{||} - D_G^{||}$.

In summary, the morphology and distribution of chiral crossing points in the two SPNs collectively influence how Ag-NPs react to the incident probe beam, as indicated by the results from Fig. 20. Based on the data from Fig. 13 and the analysis of Fig. 16, we find that the induced morphology in the samples significantly influences the optical activity. For instance, at an angle of $\alpha = 45^\circ$ where the dichroism is negative, the dissymmetry factor reaches its maximum value. Notably, this enhancement is more pronounced in the case of bi-periodic C-SPNs compared to mono-periodic ones. It should be mentioned that at an angle $\alpha = 45^\circ$, the average size of Ag-NPs and the roughness of the samples are minimal compared to the other samples made with different angles α (Fig. 9).

Conclusion

In our study, we investigated optical gyrotropy induced in the *Ag/AgCl/glass* photosensitive thin film system by interacting with two linearly polarized laser beams of different polarization vectors and wavelengths. We found that generating *bi-periodic nanostructures* (crisscrossed self-organized gratings with different periods) in light-sensitive waveguide thin films enhances the optical rotation power compared to *mono-periodic nanostructures* (crisscrossed self-organized gratings with the same periods). AFM studies, absorption spectroscopy, ellipsometry, and optical rotation measurements confirmed these results. Notably, our samples achieved up to a *7° rotation* of the probe beam's polarization plane (Fig. 18a), remarkable for a thin photonic material (*total thickness ~ 65 nm*) working in the visible spectrum. The morphology of the building blocks in the C-SPNs and the induced anisotropy of the samples are interrelated and play a crucial role in determining the magnitude and direction of the optical rotation power. The bi-periodicity increases sample anisotropy, facilitating the formation of chiral building blocks and enhancing optical rotation power. Overall, our work offers a relatively simple method for preparing optically active thin films with controllable rotation, making it advantageous for practical applications.

Acknowledgments

The authors would like to thank Prof. Yaser Abdi for his technical support of PVD depositions, from the Department of Physics of the University of Tehran, Iran. A. Nahal also wishes to thank Dr. M.F. Miri from the Department of Physics of the University of Tehran, Iran, for his valuable discussions. The presented research was funded by the Ph.D. programs of the Department of Physics, College of Science at the University of Tehran, Iran.

Authors' contributions

Arashmid Nahal was responsible for the conception, experimental design, data analysis, manuscript writing, and composition of the research. Ozra Kiasatfar was responsible for sample preparation, all measurements, AFM images, and data collection.

Availability of data and materials

The experimental data, calculations, and simulations that support the findings of this study are available from the corresponding author upon reasonable request.

Declarations

Ethical Approval and consent to participate

We did not use any human tissue in our experiments.

Competing interests

The authors have no conflict of interest to declare that is relevant to the content of this article.

Received: 9 June 2024 Accepted: 20 August 2024
Published online: 03 September 2024

References

Abdi Y, Mohajerzadeh S, Ezatollah A (2010) Modeling catalyst nucleation for carbon nanotube growth by chemical-vapor and plasma-enhanced chemical-vapor deposition methods. J. Nanopart. Res. 12:521–528

Ageev LA, Miloslavsky VK (1995) Photoinduced effects in light-sensitive films. Opt. Eng. 34:960–972

Ageev LA, Miloslavsky VK, Nahal A (1997) Study of spontaneous grating formation in photosensitive films by means of small-angle scattering. Pure Appl. Opt. 7:L1–L5

Ageev LA, Miloslavsky VK, Nahal A, Shpilevoy Y (2000) Spontaneous gratings in light-sensitive AgCl-Ag films formed by a normally incident circularly polarized focused laser beam. Opt. Commun. 173:269–276

Ashkin A (1970) Acceleration and trapping of particles by radiation pressure. Phys. Rev. Lett. 24:156–159

Barron LD (2004) Molecular light scattering and optical activity, 2nd edn. University Press, Cambridge

Fan Z, Govorov AO (2010) Plasmonic circular dichroism of chiral metal nanoparticle assemblies. Nano Lett 10:2580–2587

https://laser.physics.sunysb.edu/kristine/report/index.html
Jefimovs K, Saito N, Ino Y, Vallius T, Vahimaa P, Turunen J, Shimano R, Kauranen M, Svirko Y, Kuwata-Gonokami M (2005) Optical activity in chiral gold nanogratings. Microelectron. Eng. 78–79:448–451
Jensen TR, Duval ML, Kelly KL, Lazarides AA, Schatz GC, Van Duyne RP (1999) Nanosphere lithography: effect of the external dielectric medium on the surface plasmon resonance spectrum of a periodic array of silver nanoparticles. J. Phys. Chem. B 103:9846–9853
Kalachyova Y, Lyutakov O, Goncharova I, Svorcik V (2015) Artificial chirality induced in doped polymer by irradiation with circularly polarized excimer laser light. Opt. Mater. Express 5(12):2761–2767
Kashani S, Nahal A (2017) The role of coupled nanoplasmon excitation in growth mechanism of laser-induced self-organized nanostructures in AgCl-Ag waveguide thin films. Plasmonics 12:1305–1316
Kildishev AV, Boltasseva A, Shalaev VM (2013) Planar photonics with metasurfaces. Science 339:1232009
Kresin VV (1995) Collective resonances in silver clusters—role of d electrons and the polarization-free surface-layer. Phys. Rev. B 51:1844
Kriebig U, Vollmer M (1995) Optical properties of metal clusters. Springer, Berlin
Kuwata-Gonokami M, Saito N, Ino Y, Kauranen M, Jefimovs K, Vallius T, Turunen J, Svirko Y (2005) Giant optical activity in quasi-two-dimensional planar nanostructures. Phys. Rev. Lett. 95:227401
Li Z, Kang L, Lord RW, Park K, Gillman A, Vaia RA, Schaak RE, Werner DH, Knappenberger KL Jr (2022) Plasmon-mediated chiroptical second harmonic generation from seemingly achiral gold nanorods. ACS Nanoscience Au 2(1):32–39
Miloslavsky VK, Ageev LA, Nahal A (1998) Peculiarities of spontaneous-gratings formation in light-sensitive films under elliptically polarized laser radiation. Canadian J. Phys. 76:77–85
Miloslavsky VK, Nahal A, Ageev LA (1998) Peculiarities of spontaneous grating formation in photosensitive films under linearly and circularly polarized radiation. Opt. Commun. 147:436–442
Miloslavsky VK, Nahal A, Ageev LA (1999) Peculiarities of spontaneous gratings formation on the radiative modes under circularly polarized radiation. Opt. Commun. 164:269–276
Murai S, Tsujiguchi T, Fujita K, Tanaka K (2011) Enhanced form birefringence of metal nanoparticles with anisotropic shell mediated by localized surface plasmon resonance. Opt. Express 19:23581
Nahal A, Kashani S (2017) Optical chirality in AgCl-Ag thin films through formation of laser-induced planar crossed-chain nanostructures. J. Appl. Phys. 122:103103
Nahal A, Talebi R (2014) Ellipticity-dependent laser-induced optical gyrotropy in AgCl thin films doped by silver nanoparticles. J. Nanopart. Res. 16:2442
Nahal A, Miloslavsky VK, Ageev LA (1998) Influence of photoinduced gyrotropy on the formation of spontaneous periodic structures in light-sensitive AgCl-Ag thin films. Opt. Commun. 154:234–242
Nahal A, Mostafavi-Amjad J, Ghods A, Khajehpour MRH, Reihani SNS, Kolahchi MR (2006) Laser induced dendritic micro-structures in Ag^{+}-doped glasses. J. Appl. Phys. 100:053503
Nahal A, Asaakareh B, Miri MF (2019) Temporal evolution of photoinduced optical chirality in nanostructured light-sensitive waveguide thin films: simultaneous excitation of TE_0 and TE_1 modes. J. Appl. Phys. 125:123101
recent advances in their synthesis and applications (2022) W. Wu and. Pauly, Chiral plasmonic nanostructures. Mater. Adv. 3:186–215
P. Atkins and R. Friedman, Molecular quantum mechanics (Oxford Univ. Press, 4th Ed., 2005).
Schaferling M (2017) Chiral nanophotonics: chiral optical properties of plasmonic systems, Springer Series in Optical Sciences, vol 205. Springer, Switzerland
Svirko YP, Zheludev NI (1998) Polarization of light in nonlinear optics. Wiley, Chichester
Talebi R, Nahal A, Bashouti MY, Christiansen SH (2014) Optical nano-structuring in light-sensitive AgCl-Ag waveguide thin films: wavelength effect. Opt. Express 22:30669–30682
Tamir T (1979) Integrated Optics. Springer, Berlin
Tanaka K, Fujita K, Murai S, Meng X, Moriguchi Y, Komine T (2012) Surface plasmon-enhanced optical properties of composite materials containing metal nanoparticles: birefringence and laser oscillation. ECS Trans 50:85
Valev VK, Baumberg JJ, Sibilia C, Verbiest T (2013) Chirality and chiroptical effects in plasmonic nanostructures: fundamentals, recent progress, and outlook. Adv. Mater. 25:2517–2534
Varminsky MV, Ageev LA, Miloslavsky VK (1998) Observing diffraction from photo-induced TE gratings in the process of their formation in thin films. J. Opt. 29:253–258
Zhang B, Tan D, Liu X, Tong L, Kazansky PG, Qiu J (2019) Self-organized periodic crystallization in unconventional glass created by an ultrafast laser for optical attenuation in the broadband near-infrared region. Adv. Opt. Mat. 7(20):1900593
Zhang B, Liu X, Qiu J (2019) Single femtosecond laser beam induced nanogratings in transparent media - mechanisms and applications. J. Materiomics 5(1):1–14
Zhang B, Wang Z, Tan D, Qui J (2023) Ultrafast laser-induced self-organized nanostructuring in transparent dielectrics: fundamentals and applications. PhotoniX 4:24
Z. Hirbodvash, S. Kashani, M. F. Miri, and A. Nahal, Formation of self-organized gratings in AgCl thin film, doped by silver nanoparticles, under off-normal incidence of He-Ne laser beam, in Proceedings of 1st National Conference on Nanostructures and Graphene (Central Branch of Azad University, Tehran, Iran) April 2015, (in Persian).

Publisher's Note